Dike propagation through layered rocks

Taisne, B.; Jaupart, C.

2009

Taisne, B., & Jaupart, C. (2009). Dike propagation through layered rocks. Journal of Geophysical Research, 114.

https://hdl.handle.net/10356/87710

https://doi.org/10.1029/2008JB006228

Dike propagation through layered rocks

B. Taisne[1] and C. Jaupart[1]

Received 24 November 2008; revised 25 May 2009; accepted 8 July 2009; published 19 September 2009.

[1] Dike penetration through a succession of upper crustal layers with different densities is studied with a new numerical code. For an individual layer to significantly affect dike ascent, its thickness must be of order 1 when scaled to the characteristic length-scale for the inflated nose region that develops below the dike tip. This characteristic length is $L^* \propto (\mu Q)^{1/6} (G/(1-\nu))^{1/2} (\Delta\rho g)^{-2/3}$, where μ and $\Delta\rho$ are the viscosity and buoyancy of magma, G and ν are elastic moduli for the encasing rocks, Q is the magma flow rate and g gravity. For basaltic dikes, L^* is $\approx$1 km, which is of the same order of magnitude as the typical thickness of sedimentary strata and volcanic deposits. In such conditions, dike ascent proceeds irregularly, with large changes of velocity and width at an interface. Scaling laws for the ascent rate and dike width are derived. Penetration through low-density layers is determined by a local buoyancy balance in the inflated nose region of the dike, independently of the total buoyancy of the magma column between source and tip. In such conditions, a dike develops an internal overpressure that may be large enough to generate a horizontally propagating sill. For this to occur, the thickness of the low-density layers must exceed a threshold value, which depends only on the rock strength and on the average negative buoyancy of magma. For basaltic melt, we estimate that this threshold thickness cannot be less than about 700 m and is 2 km on average.

Citation: Taisne, B., and C. Jaupart (2009), Dike propagation through layered rocks, *J. Geophys. Res.*, *114*, B09203, doi:10.1029/2008JB006228.

1. Introduction

[2] The shallow crustal environment is usually made of many different strata with different densities. In such conditions, magma buoyancy may change by large amounts and may become negative. Important consequences for magma ascent include changes of velocity and dike dimensions, and the formation of a sill, such that a vertical dike feeds a horizontally propagating fracture. These have important implications for the monitoring of active volcanoes and for the formation of magma storage zones in the upper crust.

[3] Few studies have accounted for the dynamics of dike propagation in a stratified environment. Gudmundsson and coauthors have drawn attention to the layering that typifies sedimentary and volcanic settings and to its important effects on the characteristics of deformation generated by an input of magma [*Gudmundsson and Brenner*, 2001; *Gudmundsson*, 2005; *Gudmundsson and Philipp*, 2006]. These complex models, however, rely on a hydrostatic pressure distribution or a constant overpressure in the magma column and hence do not address the dynamics of magma ascent. Theoretical analysis has been restricted to continuous stratification, such that the density of encasing rocks decreases linearly with height above source [*Lister and Kerr*, 1991; *Lister*, 1991].

[4] To our knowledge, propagation through layered media has only been studied in the laboratory [*Rivalta et al.*, 2005; *Kavanagh et al.*, 2006]. These studies have dealt with only two layers and a restricted range of layer thicknesses. In contrast, the natural crustal environment involves a large number of strata and it may not be sufficient to consider that penetration through each individual layer proceeds independently of the neighboring layers.

[5] In the upper crust, the largest change of physical properties occurs when going from the crystalline basement to the sedimentary cover. Important observations are that many sills get intruded within the sedimentary strata, above the basement interface, and that no particular lithology acts as a barrier or a favorite host [*Francis*, 1982]. This indicates that sill inception is not determined by the intrinsic physical properties of a particular rock in the sequence. Figure 1 shows a vertical density profile through the sedimentary layers of the Michigan [*Hinze et al.*, 1978] and emphasizes the intricate variations that occur. In such an environment, basaltic magma with density ρ_m = 2700 kg m^{-3} would be alternatively buoyant and negatively buoyant. Given that buoyancy is a volume force, a basaltic dike may overshoot a neutral or negative buoyancy layer and it is unlikely that its behavior is determined by the local properties of a single lithological level.

[6] The present study complements earlier ones. *Lister* [1991] considered the steady state propagation of a dike with a linear decrease of buoyancy, such that buoyancy becomes negative at some level. He showed that, below the level of neutral buoyancy, magma buoyancy is balanced by

[1]Equipe de Dynamique des Fluides Géologiques, Institut de Physique du Globe de Paris, Paris, France.

0148-0227/09/2008JB006228$09.00

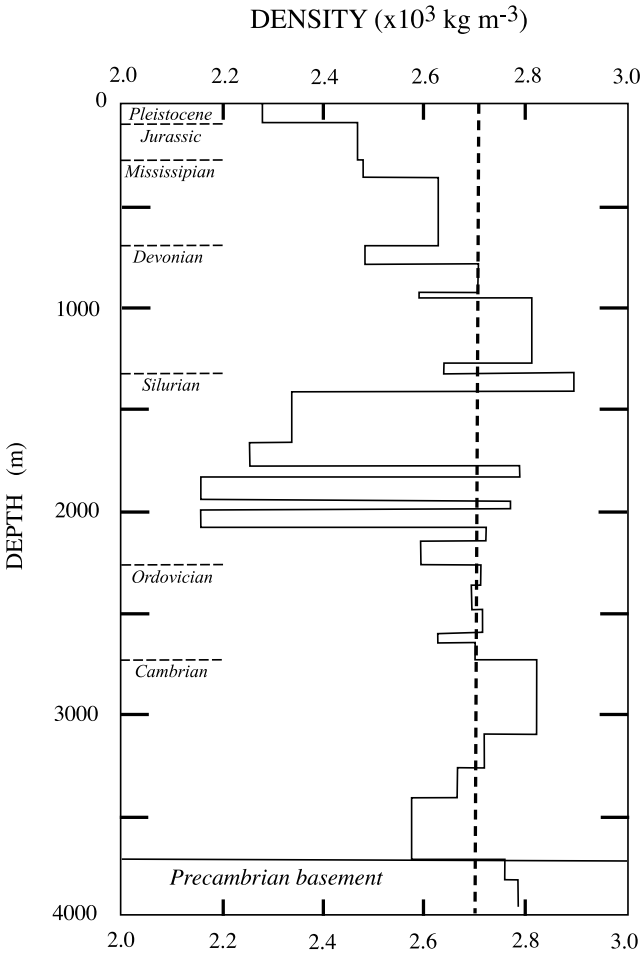

Figure 1. Vertical distribution of density through the sedimentary rocks of the Michigan basin from *Hinze et al.* [1978]. The vertical dashed line corresponds to the density of a typical basaltic melt.

the viscous pressure drop due to the flow of magma within the fracture. Thus the maximum height of propagation is not sensitive to the total buoyancy integrated over the whole magma column and is controlled by local conditions in the inflated nose region below the dike tip. In this paper, we study dike propagation through a layered medium and focus on the influence of the thickness of individual layers. We develop simple scaling laws that describe how the width and velocity of a dike change as it penetrates through an upper layer with a different density. We then investigate models involving several layers. We show that, in such complex settings, dike behavior is indeed determined by local buoyancy considerations. We conclude the paper with a discussion of sill inception.

2. Stratified Media

[7] In this paper, dike propagation is studied within the framework of linear elastic fracture mechanics because it is appropriate at shallow crustal levels and because it has been studied extensively [*Lister*, 1990; *Lister and Kerr*, 1991; *Rubin*, 1995; *Menand and Tait*, 2002]. Furthermore, this allows benchmark comparisons with well-posed solutions. Stratification can take many different forms and involves several physical properties. For our present purposes, four types of properties are involved: the elastic moduli, fracture toughness, density and the behavior of the interface (i.e. whether it is welded or allows slippage). In a careful study of a large number of dikes in the Ramon area, Israel, *Baer* [1991] demonstrated that bedding plane slippage plays a minor role, and this effect will not be accounted for in this paper. We return to this issue in a discussion section at the end.

[8] Elastic moduli do not vary by large amounts among common rock types. As shown by Table 1, they lie within a range of 10–60 GPa with rare exceptions. Young's modulus takes small values in a few sandstones and limestones in association with anomalously high porosity. With increasing confining pressures, the elastic moduli of these rocks increase due to the closure of cracks and pores. For example, values of Young's modulus for the Leadville, Colorado, limestone are 11 and 17 GPa at confining pressures of 100 and 200 MPa, respectively (corresponding to depths of about 3 and 6 km [*Touloukian and Ho*, 1981]). Such values are lower than those of crystalline basement by a factor of about 3 on average. There are significant amounts of overlap between the ranges for the different rock types, however, implying that an accurate quantitative model can only be made on a case-by-case basis after evaluation of the local physical properties in the area of interest. In the vicinity of an interface, it takes differences of elastic properties of about one order of magnitude to generate marked differences in dike behavior, because of the constraint that the displacement be continuous at the interface [*Bonafede and Rivalta*, 1999]. Thus variations of elastic moduli are not expected to alter greatly the dynamics of dike propagation in the vast majority of geological cases. We shall show that local hydrostatic considerations can go a long way and they can be extended to layers with different elastic moduli if need be, using, for example, the method of *Bonafede and Rivalta* [1999].

[9] Values for the fracture toughness are not known with precision, but they are small when scaled to magmatic dike characteristics [*Lister and Kerr*, 1991]. This point is discussed in detail in Appendix A. In geological conditions, as shown by *Lister* [1990] and by our numerical results in Appendices B and C, the fracture toughness of encasing rocks has no significant influence on the length of the nose region and affects the shape and width of the dike near the tip only weakly. We shall argue and demonstrate with our calculations that the nose length is the critical parameter for dike penetration through a layer of finite thickness.

Table 1. Mean Values of the Young's Modulus E, Poisson's Ratio ν, and Density ρ for Different Kinds of Rocks

Name	Young's Modulus E (GPa)	Poisson's Ratio ν	Density ρ (kg m^{-3})
Basalt (solid)	28–86	0.16–0.21	2590 ± 339
Gneiss	19–71	0.06–0.12	2700 ± 90
Granite	17–61	0.10–0.39	2660 ± 50
Shale	12–47	0.11–0.20	2340 ± 379
Sandstone	8.4–12.4[a]	0.14–0.42	2320 ± 149
Limestone	17.3–27.2[a]	0.14–0.48	2670 ± 114

[a]Values for 200 MPa confining pressure, corresponding to rocks below Earth's surface with some cracks closed [*Touloukian and Ho*, 1981].

[10] In contrast to the fracture toughness and to the elastic moduli, magma buoyancy varies by large amounts in continental crustal rocks: for basaltic melt with a density of 2700 kg m^{-3}, it lies within a range of about [−500, 200] kg m^{-3} (Table 1, Figure 1). Thus we expect that changes of buoyancy have a large effect on dike propagation, if only because they encompass positive and negative values. It is clear from Table 1 that the most important change of country rock properties occurs at the interface between crystalline basement and a sedimentary cover. One important feature of sedimentary rocks, however, is that they are layered, with densities that change over rather small vertical distances, as emphasized by Figure 1. We shall show that such intricate variations have a marked effect on dike penetration.

3. Governing Equations

[11] We treat the opening of a fracture in two-dimensional dimensions, with vertical coordinate z positive upward ($z = 0$ at Earth's surface) and horizontal coordinate x. Ignoring the negligible atmospheric pressure, the lithostatic pressure in encasing rocks of density ρ_s is $P_{Lith} = -\rho_s g z$.

3.1. Magma Flow

[12] Within the magma, pressure P may be decomposed into an overpressure P_e, which drives deformation of the fracture walls, and a lithostatic component:

$$P = P_{Lith} + P_e. \tag{1}$$

[13] We assume that magma behaves as an incompressible fluid with density ρ_m and viscosity μ. For a thin and vertical fracture, flow occurs at small Reynolds number and one can use lubrication theory, so that the vertical momentum equation reduces to:

$$0 = -\frac{\partial P}{\partial z} + \mu \frac{\partial^2 w}{\partial x^2} - \rho_m g, \tag{2}$$

where w is the vertical velocity. The volume flux of magma at depth z is:

$$\phi(z) = \int_{-h}^{h} w(z,x)dx, \tag{3}$$

where the dike width is $2h$. Using equations (2) and (3) leads to:

$$\phi = -\frac{2}{3\mu} h^3 \left(\frac{\partial P}{\partial z} + \rho_m g \right). \tag{4}$$

Substituting for P into the flux equation (4), we obtain:

$$\phi = -\frac{2}{3\mu} h^3 \left(\frac{\partial P_e}{\partial z} - \Delta\rho g \right), \tag{5}$$

where $\Delta\rho = \rho_s - \rho_m$ is the magma buoyancy. Volume conservation (equivalent to mass conservation for the incompressible fluid) is written as:

$$2\frac{\partial h}{\partial t} = -\frac{\partial \phi}{\partial z}. \tag{6}$$

To illustrate the dynamics of dike propagation as magma buoyancy changes, we shall use the driving pressure, P_d, such that:

$$\frac{\partial P_d}{\partial z} = \frac{\partial P}{\partial z} + \rho_m g. \tag{7}$$

3.2. Elastic Deformation

[14] For a dike extending from a distant source ($z \to -\infty$) to a tip located at $z = z_f$, half-width h and overpressure P_e are related to one another through the following equation [*Muskhelishvili*, 1953; *Weertman*, 1971]:

$$P_e(z) = -\frac{G}{1-\nu}\frac{1}{\pi}\int_{-\infty}^{z_f} \frac{\partial h}{\partial \xi}\frac{d\xi}{\xi - z}, \tag{8}$$

where G is the shear modulus and ν is Poisson's ratio. One can invert this equation to solve for the dike width as a function of P_e. Integrating by parts leads to the following equation for h [*Spence et al.*, 1987]:

$$h(z) = \frac{1-\nu}{G}\frac{1}{\pi}\int_{-\infty}^{z_f} k(z_f, z, \xi) P_e(\xi) d\xi, \tag{9}$$

where kernel $k(z_f, z, \xi)$ is such that:

$$k(z_f, z, \xi) = \ln\left| \frac{\sqrt{z_f - z} + \sqrt{z_f - \xi}}{\sqrt{z_f - z} - \sqrt{z_f - \xi}} \right|. \tag{10}$$

3.3. Boundary Conditions

[15] Ahead of the dike tip, the normal elastic stress has a singularity, such that:

$$P_e(z) \sim -\frac{K}{2\sqrt{z - z_f}}, \text{ for } z > z_f, \tag{11}$$

where K is the stress intensity factor. For a propagating dike, the stress intensity factor is set equal to a material property called the fracture toughness, K_c. This specifies the shape of the dike near the tip [*Muskhelishvili*, 1953; *Weertman*, 1971]:

$$h \sim \frac{1-\nu}{G} K_c \sqrt{2(z_f - z)}, \text{ for } z \to z_f. \tag{12}$$

Equations (9)–(12) can be combined [*Lister*, 1990]:

$$K_c\sqrt{2} = \frac{2}{\pi}\int_{-\infty}^{z_f} \frac{P_e(\xi)}{\sqrt{z_f - \xi}} d\xi. \tag{13}$$

3.4. Dimensional Analysis

[16] We consider that magma is fed into the dike at a constant volumetric rate Q (in the present two-dimensional framework, we refer to a volumetric rate per unit fissure length, expressed in units of $m^3\ s^{-1}\ m^{-1}$, i.e. $m^2\ s^{-1}$). For a dike extending over large vertical distances, very small magma overpressures are sufficient to drive elastic defor-

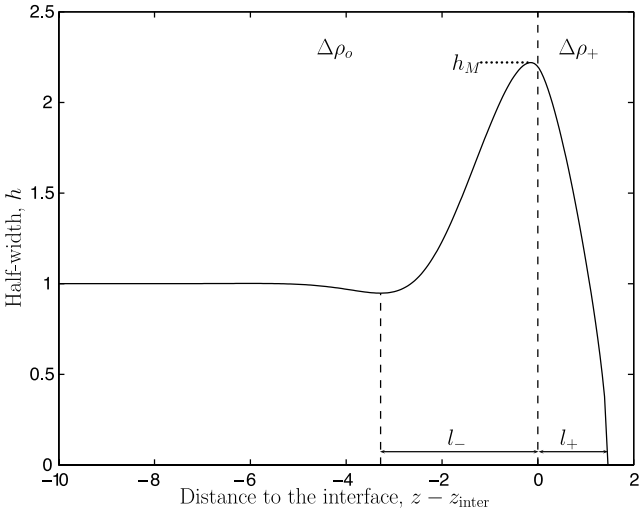

Figure 2. Definition of the characteristics of a dike going through a density interface located at $z = z_{\text{inter}}$. l_+ and l_- stand for the lengths of the nose region above and below the interface, respectively. Total nose length is $l = l_- + l_+$, and nose width is h_M. For typical geological values, a dimensionless half-width of one corresponds to 1 m and a dimensionless distance of one corresponds to 1 km (see text for details).

mation. Thus far from the tip, the dominant force balance in the thin tail region is between magma buoyancy and viscous head loss. This defines scale h^* for the dike half width [*Lister and Kerr*, 1991]:

$$h^* = \left[\frac{3\mu Q}{2\Delta\rho g}\right]^{1/3}. \tag{14}$$

This argument also leads to a velocity scale:

$$c^* = \frac{Q}{2h^*}. \tag{15}$$

As shown by *Lister and Kerr* [1991] the dominant dynamical balance in the nose region is between buoyancy and the magma overpressure driving elastic deformation (see also Appendix A). This introduces length scale L^*, such as buoyancy applied over L^* acts to open a fracture of width h^*:

$$\Delta\rho g L^* = \Delta P^* = \frac{G}{1-\nu}\frac{h^*}{L^*}, \tag{16}$$

which defines pressure scale ΔP^*. Solving for L^* yields:

$$L^* = \left[\frac{Gh^*}{(1-\nu)(\rho_s - \rho_m)g}\right]^{1/2} = \left(\frac{3\mu Q}{2}\right)^{1/6}\left(\frac{G}{1-\nu}\right)^{1/2}(\Delta\rho g)^{-2/3}. \tag{17}$$

Combining these pressure and length scales (equations (16)–(17)), one obtain a scale for the stress intensity factor [*Lister and Kerr*, 1991]:

$$K^* = \Delta P^*\sqrt{L^*} = \Delta\rho g (L^*)^{3/2}. \tag{18}$$

Typical values of the physical properties and control variables for basaltic magmas are $\Delta\rho = 200$ kg m^{-3}, $\nu = 0.2$, $G = 10^{10}$ Pa, $\mu = 10^2$ Pa s and $Q = 2$ m^3 s^{-1} m^{-1} [*Thordarson and Self*, 1993]. For these, the dike width $2h^*$ is $\approx$1 m and the nose region extends over length $\approx 4L^* \approx 6$ km (Appendix C). In the following, all variables will be made dimensionless with these scale factors, unless specified otherwise, and will be written without special symbols for convenience.

[17] As emphasized by *Lister* [1990], the tail region of the dike, below the nose, is such that the fracture is kept open by negligible elastic stresses and hence such that buoyancy is balanced by viscous head loss. The wider nose region is such that the viscous head loss is small and hence such that elastic deformation is driven by the local buoyancy. Thus the characteristics of dike deformation do not depend on the total buoyancy of the vertical magma column integrated from source to tip. This indicates that dike behavior is sensitive to buoyancy changes over characteristic distance L^*, and hence that it is affected by layering in the encasing rocks if the typical layer thickness L is of the same order of magnitude as L^* (i.e. if $L/L^* \sim 1$). On the one hand, if $L/L^* \ll 1$, layering is on a scale that is too small for propagation to be sensitive to individual layers. In this case, it is sufficient to deal with an average density for the set of layers. If, on the other hand, $L/L^* \gg 1$, the dike is only subjected to a few discrete steps during ascent and propagation through each separate layer proceeds as in an infinite medium. In the intermediate case, one expects complex behavior. For the parameter values listed above, $L^* \approx 1$ km, so that layering must be in a range of a few hundred meters to a few kilometers for dike ascent to be in the intermediate regime. Such a range is relevant to strata in a sedimentary basin (e.g., Figure 1) and to volcanic successions in an active region.

[18] Figure 2 shows the various variables that will be used to describe dike behavior in the vicinity of a density interface: penetration length l_+, which is equal to the distance between the dike tip and the interface, maximum dike width h_M, maximum internal overpressure $P_{e\ \max}$ and finally the length of the nose region $l = l_+ + l_-$. By definition, the nose region extends between the dike neck, where the dike thickness has a local minimum, and the dike tip located at $z = z_f$. All the calculations that are reported below were made for $K_c/K^* = 1$. In Appendices B and C, however, we report on calculations made for a range of values for the stress intensity factor in order to assess the performance of the numerical code against the analytical results of *Lister* [1990].

4. Dike Propagation Through a Density Interface

[19] Here we describe how a dike penetrates through a two-layer system involving two different densities. The upper layer extends over a large vertical distance so that the dike can fully adjust to the change of density that occurs at the interface. In other words, we consider cases such that $L/L^* \gg 1$.

4.1. Penetration Through a Medium With Reduced Buoyancy

[20] We consider first an upper layer that has a lower density than the underlying medium, but such that magma is still buoyant above the interface. For a given flux of magma

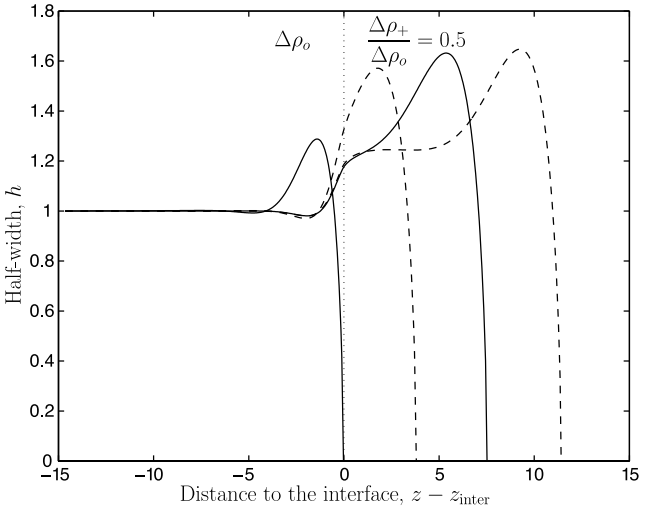

Figure 3. The shape of a dike penetrating into a layer with reduced buoyancy. The interface lies at $z = z_{\text{inter}}$ (vertical dotted line). Results are shown at a fixed time interval $\Delta t = 4.79$. Note that the nose region rapidly adjusts to new dimensions in the upper layer. (Calculations are made for a dimensionless stress-intensity factor equal to 1, i.e., $K_c/K^* = 1$).

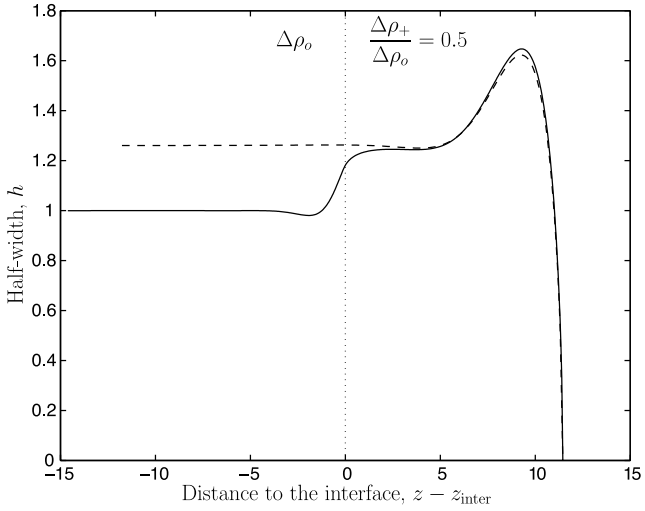

Figure 4. The shape of a dike that has penetrated in an upper layer of reduced buoyancy (in dimensionless values). The base of this layer is at $z = z_{\text{inter}}$ (vertical dotted line). The dashed curve shows the steady state shape of a dike that propagates through an infinite medium with the density of the upper layer.

at the source, one expects that dike propagation will slow down and that the dike will become wider as it rises through the upper layer. For the sake of example, we consider that magma buoyancy drops by a factor of two, such that:

$$\frac{\Delta\rho_+}{\Delta\rho_o} = 0.5. \tag{19}$$

Solutions for this case are shown in Figure 3. The behavior of the dike is easily understood by considering that, at large distances from the interface, the dike behaves as in an infinite medium with different properties. Thus using the scalings developed above, it adjusts to a new width h_+ which may be deduced from h_o in the lower medium through the following relationship:

$$h_+ = h_o\left(\frac{\Delta\rho_o}{\Delta\rho_+}\right)^{1/3}. \tag{20}$$

We compare in Figure 4 the shape of the dike far above the interface to that of a steady state dike through an infinite medium with the same reduced buoyancy as the upper layer. The two shapes are almost indistinguishable. More revealing is the behavior of the dike as it goes through the interface. As shown in Figure 3, the dike starts swelling as soon as it starts intruding the upper layer. One consequence is that it slows down markedly, as the same magma flux must feed an inflating nose region. Using the scaling relationships $c^* = Q/2h$ and $h \propto (\Delta\rho)^{-1/3}$, velocity is expected to tend toward the steady state value in the new encasing medium with reduced buoyancy:

$$c_+ = c_o\left(\frac{\Delta\rho_+}{\Delta\rho_o}\right)^{1/3}. \tag{21}$$

In dimensionless values, $c_o = 1$ in the lower layer and we deduce that $c_+ = 0.79$ in the upper layer. In an initial phase such that the nose region protrudes into the upper layer, the velocity drops rapidly as the nose region swells (Figure 5). The ascent velocity drops to small values below c_+ and then increases toward this value as the dike adjusts to its new environment. These velocity variations occur over a dimensionless distance of ≈10, corresponding to ≈10 km for the parameters given above.

[21] We may draw two important implications from these results. One is that, if detected by a seismic array over a volcanic center, the slowing down of magma ascent may not

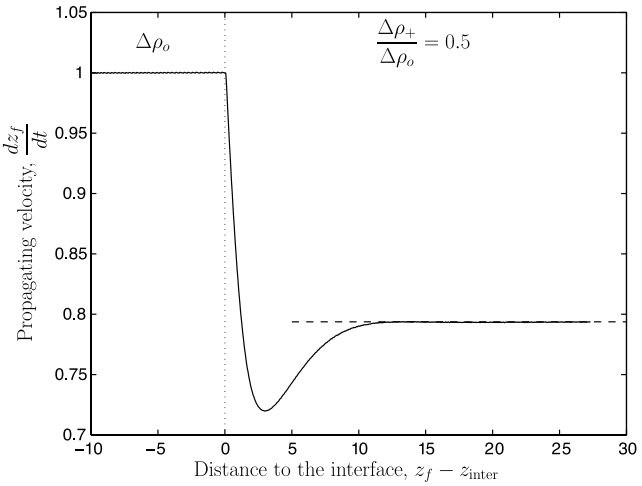

Figure 5. Changes of ascent velocity as a dike penetrates into a layer with reduced buoyancy. The base of this layer is at $z = z_{\text{inter}}$ (vertical dotted line). The dashed line shows the steady state velocity in the upper layer. Note that the velocity adjustment phase is spread over a large vertical distance above the interface.

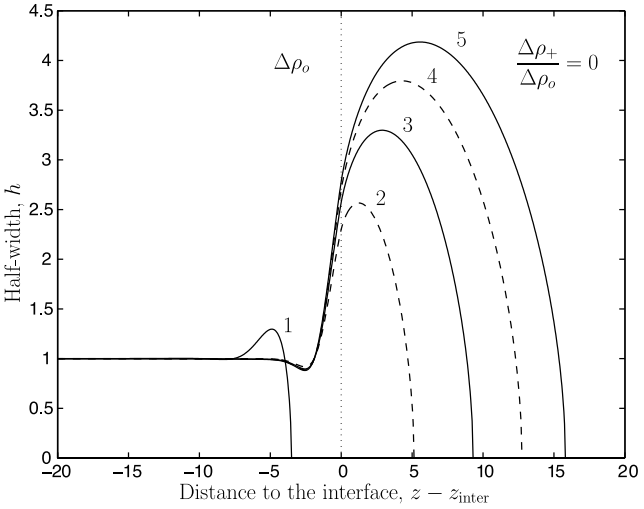

Figure 6. Shape of a dike that penetrates into a layer with neutral buoyancy ($\Delta t_{1-2} = \Delta t_{2-3} = \Delta t_{3-4} = \Delta t_{4-5} = 14.364$). The base of this layer is at $z = z_{\text{inter}}$ (vertical dotted line). Magma pressure profiles for times (1) and (5) are given in Figure 7 below. Note that the dike inflates above the interface and that it penetrates over large vertical distances above the interface. Calculations are made for $K_c/K^* = 1$.

necessarily herald the cessation of intrusion or the injection of a horizontal sill. As shown by Figure 5, the velocity decrease may in fact be followed by an acceleration phase. A proper interpretation of a seismic sequence during volcanic unrest must therefore rely on detailed knowledge of the shallow geological environment (including variations of elastic properties if need be). Another implication is that the upper layer must be thicker than some threshold value for the dike to fully adjust to the new surroundings. For the density change used in the calculations in Figure 5 and the typical eruption parameter values given above, the upper layer must be at least 10 km thick for dike propagation to resume at a new steady rate. We expect that dike-induced seismicity at shallow depth exhibits complex patterns in both space and time due solely to density stratification, without any change of magma supply or magma composition.

4.2. Dike Penetration at Neutral Buoyancy

[22] Many models of magma reservoir formation rely on emplacement at a neutral buoyancy level. In reality, one may not expect magma to encounter rocks with exactly the same density. Furthermore, as we have already hinted at in the previous section, one is likely to deal with stratified rock sequences on the scale of a few hundred meters. We shall investigate such situations below. Nevertheless, for the sake of argument, we investigate here what happens if there is such a thing as a neutral buoyancy layer.

[23] As shown in Figure 6, the dike develops a large nose region as it penetrates through a neutral buoyancy layer. Below the interface, the dike tends rapidly to a new steady state shape with a small neck at some distance of the neutral buoyancy level. Above the interface, the upper part of the dike is fed at a constant rate but it is not driven upward by buoyancy: thus the nose region swells, which induces a decrease of ascent rate. We shall develop below simple arguments to illustrate the quantitative aspects of this. The pressure distribution is illustrated in Figure 7.

[24] As noted above, the nose region above the interface is fed at rate Q. Thus its volume grows linearly with time. Assuming that this swollen region keeps the same shape and only changes dimensions, we can specify the volume using length l and width h_M (Figure 2):

$$V = Q(t - t_o) \propto Clh_M, \tag{22}$$

where t_o is some initial time such that the nose adjusts to a constant shape and C is a constant of proportionality which depends on the nose shape. Elastic stresses are small in the tail region and are only significant in the nose region. Thus the stress intensity factor at the dike tip corresponds to that for a fracture of length l. In the upper layer, there is no buoyancy force, by definition. The elastic pressure is related

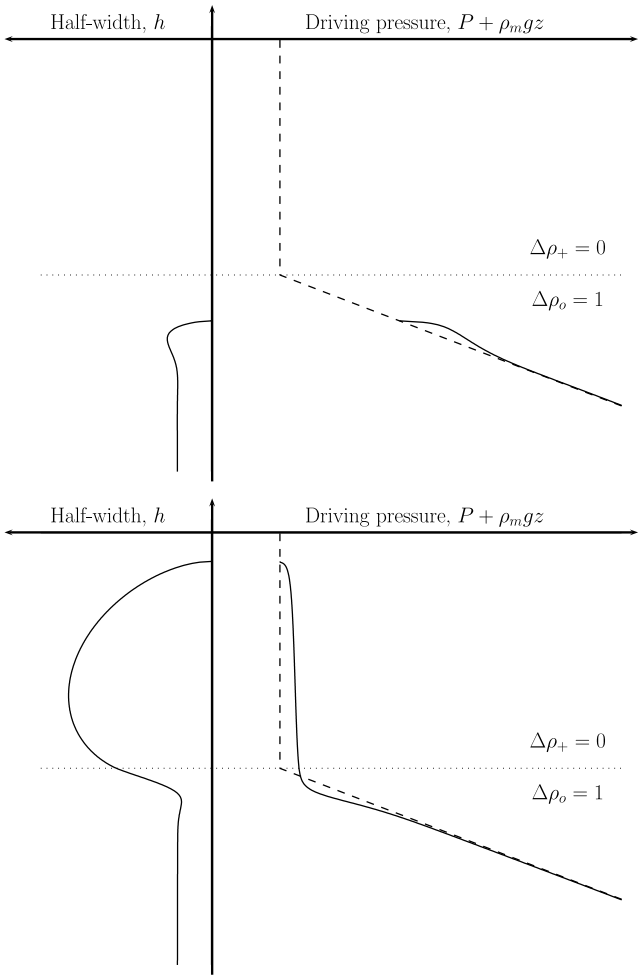

Figure 7. Half-width h and driving pressure P_d for a dike penetrating in a medium with neutral buoyancy at times (1) and (5) of Figure 6. Driving pressure is that which determines the flow rate and is defined by equation (7). Here it is shown to within an arbitrary constant. The dashed line is such that $\partial P_d/\partial z = -\Delta\rho g$, where $\Delta\rho = \rho_s - \rho_m$, corresponding to zero internal overpressure within the dike.

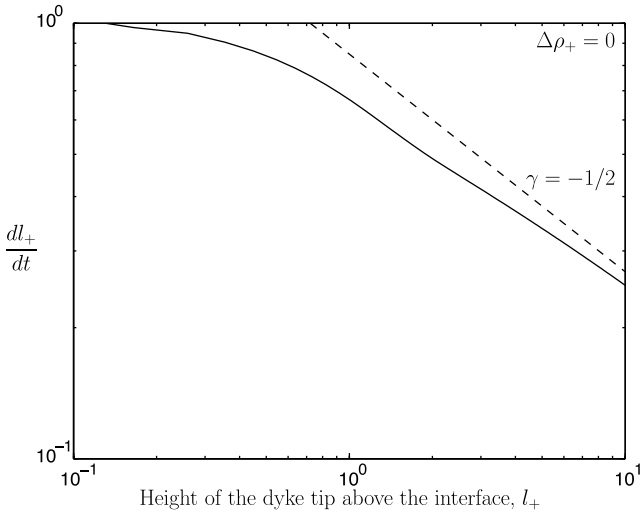

Figure 8. Ascent rate of a dike that penetrates into a layer with neutral buoyancy, as a function of distance above the interface. Dashed line: power law relationship deduced from a simple local hydrostatic model (see text, equation (26)).

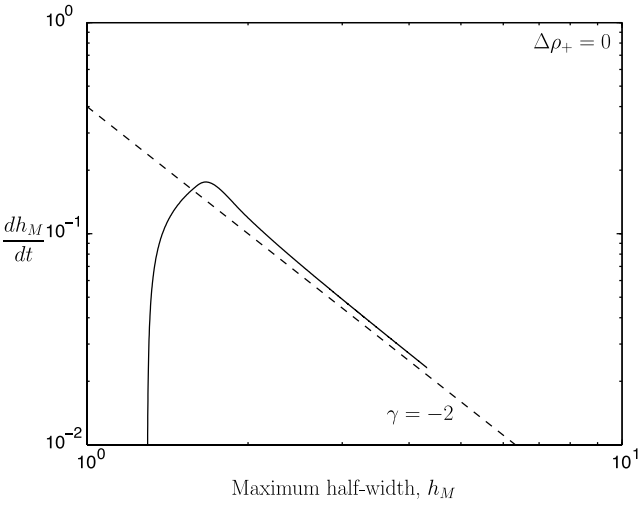

Figure 9. Time rate of change for the maximum width of a dike that penetrates into a layer with neutral buoyancy. Dashed line: power law relationship deduced from a simple local hydrostatic model (see text, equation (27)).

to width h_M through $\Delta P \approx Gh_M/l$. Thus the stress intensity constraint can be written in dimensional form as follows:

$$G\frac{h_M}{l}\sqrt{l} \sim K_c. \tag{23}$$

[25] Combining equations (22) and (23) leads to the following scaling laws for l and h_M:

$$l \propto (t - t_o)^{2/3}, \tag{24}$$

$$h_M \propto (t - t_o)^{1/3}. \tag{25}$$

By construction, these scaling laws are only valid for a nose region that has a constant shape, and hence only apply once the dike has penetrated over a significant distance in the upper layer. For comparison with the numerical results, one must specify time t_o and it is easier to use the scalings in the following form:

$$\frac{dl}{dt} \propto l^{-1/2}, \tag{26}$$

$$\frac{dh_M}{dt} \propto h_M^{-2}, \tag{27}$$

which involve power laws of the form $dX/dt \propto X^\gamma$ with different values of exponent γ. Numerical results for the nose length and width do tend to these relationships (Figures 8–9). The shape of the nose region changes as the dike goes through the interface and does not instantaneously adjust to the new conditions, implying that the results do not follow the scaling laws in early stages of penetration.

4.3. Penetration With Negative Buoyancy

[26] The last case is that of magma propagating through material that is less dense (Figure 10). For simplicity, we consider that the density contrast just changes sign at the interface, i.e. $\Delta\rho_+ = -\Delta\rho_o$. Once again, the dike rises past the interface even though its upper part is no longer buoyant, because buoyancy in the lower layer continues to drive the flow of magma. The pressure distribution is illustrated in Figure 11.

[27] In the inflated nose region, viscous stresses are small and hence the local pressure distribution is determined by a hydrostatic balance. The nose region grows both above and

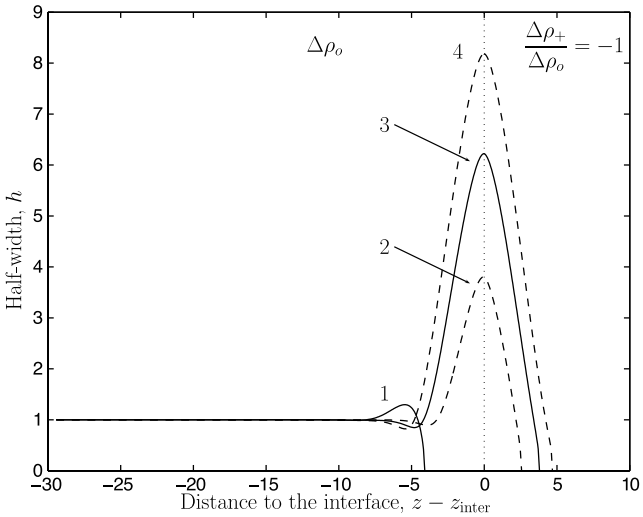

Figure 10. A dike penetrating into a layer with negative buoyancy ($\Delta t_{1-2} = \Delta t_{2-3} = \Delta t_{3-4} = 14.364$). The distributions of driving pressure at times (1) and (2) are given in Figure 11. Note that the dike is able to overshoot the interface and that it swells markedly. ($K_c/K^* = 1$).

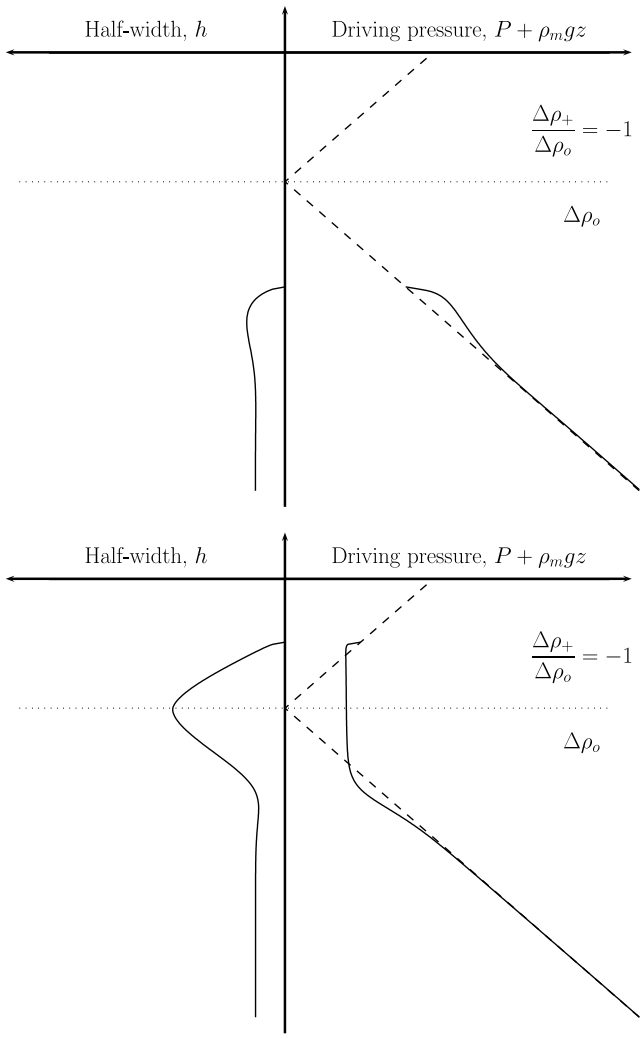

Figure 11. Half-width and driving pressure for a dike penetrating into an upper layer with negative buoyancy. Conventions are as in Figure 7. (top and bottom) The dike at time (1) and (2) of Figure 10. Note that the driving pressure is approximately constant in the inflated nose region when the dike has gone through the interface due to small viscous head loss.

below the interface, over lengths l_+ and l_- respectively (Figure 2). Thus one has:

$$|\Delta\rho_o g l_-| \sim \left|\Delta\rho_+ g l_+\right|, \tag{28}$$

and hence,

$$l_+ \sim l_- \left|\frac{\Delta\rho_o}{\Delta\rho_+}\right|. \tag{29}$$

Using $l = l_- + l_+$, we calculate dimensionless ratios l_+/l and l_-/l as function of the density contrast ratio. In the present example, we have assumed that $\Delta\rho_o = -\Delta\rho_+$, so that this argument predicts that $l_- = l_+$. Figure 12 shows that the numerical results tend toward these relationships. Here the point is again that the deformation characteristics and the magma overpressure distribution are determined by local hydrostatic considerations.

[28] To proceed further, we consider that the nose region is fed from below at rate Q, which provides a relationship between the nose length l and nose width h_M, as already noted above. We can also relate the dike width to the magma overpressure in the nose region:

$$G\frac{h_M}{l} \sim |\Delta\rho_o g l_-| \sim \left|\Delta\rho_+ g l_+\right|. \tag{30}$$

[29] We thus obtain:

$$V = Q(t - t_o) \propto h_M l_+ \left(1 + \left|\frac{\Delta\rho_+}{\Delta\rho_o}\right|\right), \tag{31}$$

$$G\frac{h_M}{l_+\left(1 + \left|\frac{\Delta\rho_+}{\Delta\rho_o}\right|\right)} \sim \Delta\rho_+ g l_+, \tag{32}$$

so that:

$$l_+ \propto (t - t_o)^{1/3} \text{ or } \frac{dl_+}{dt} \propto l_+^{-2}, \tag{33}$$

$$h_M \propto (t - t_o)^{2/3} \text{ or } \frac{dh_M}{dt} \propto h_M^{-1/2}. \tag{34}$$

[30] Numerical results tend toward these predictions (Figures 13–14). The results show that the dike penetrates well above the interface, driven by the local buoyancy of the lower nose region. Magma buoyancy in the long tail region is balanced by viscous stresses and hence does not

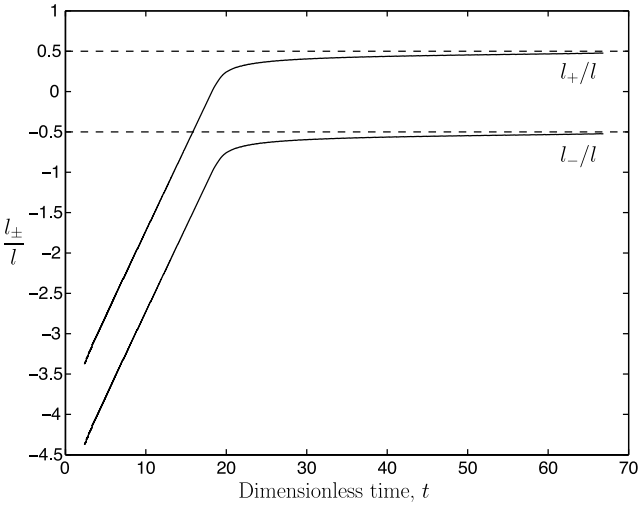

Figure 12. Vertical extents of the upper and lower parts of the head region of a dike that penetrates into a layer with negative buoyancy, as a function of time (in dimensionless values). For these calculations, buoyancy changes sign at the interface, such that $\Delta\rho_+ = -\Delta\rho_o$. Both lengths tend to the limit values predicted by a simple local hydrostatic balance (equations (28) and (29)).

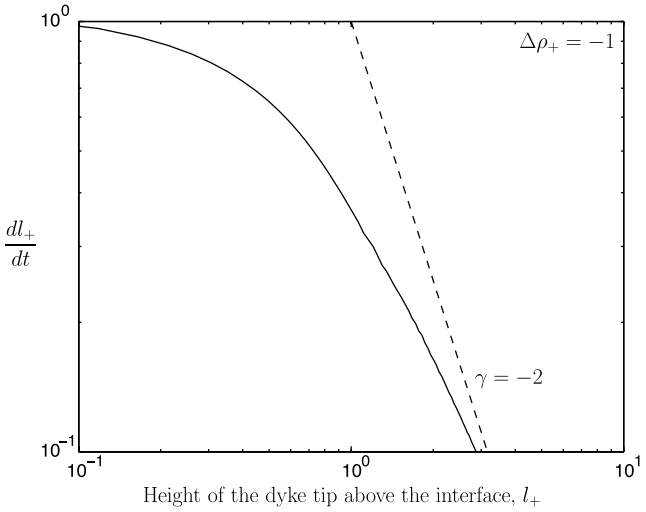

Figure 13. Velocity of a dike penetrating into a layer with negative buoyancy, as a function of distance above the interface. Dashed line: prediction of a simple hydrostatic model for the nose region (equation (33)).

contribute to the driving force for country rock deformation in the vicinity of the interface.

5. Sill Formation

[31] We are interested in cases where the internal magma overpressure is sufficient to fracture the dike walls and induce a laterally propagating sill, as illustrated in the experiments of *Rivalta et al.* [2005] and *Kavanagh et al.* [2006].

5.1. A Thin Horizon With Negative Buoyancy

[32] We first consider that the dike penetrates a thin horizon that is sandwiched between two denser layers. For illustrative purposes, we set the dimensionless density

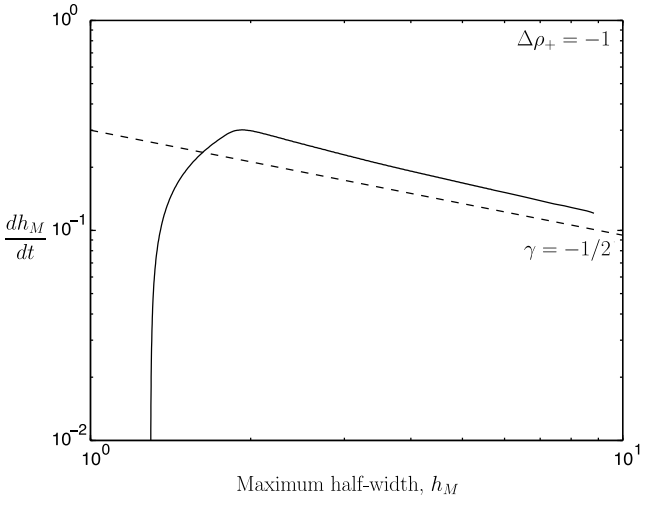

Figure 14. Time rate of change for the maximum dike width, as a function of maximum dike width for a dike penetrating into a layer with negative buoyancy. Dashed line: prediction of a simple hydrostatic model for the nose region (equation (34)).

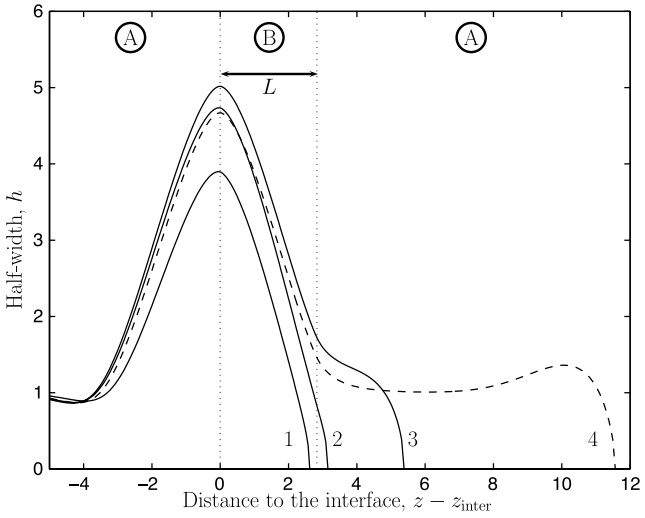

Figure 15. Dike going through a negative buoyancy horizon that is sandwiched between two denser layers. The dimensionless horizon thickness is $L = 2.840$. Materials A and B correspond to $\Delta\rho_A/\Delta\rho_o = 1$ and $\Delta\rho_B/\Delta\rho_o = -1$, respectively. Time intervals between successive profiles are $\Delta t_{1-2} = \Delta t_{2-3} = \Delta t_{3-4} = 4.788$. Driving pressure distributions for this case are illustrated in Figure 17. Note that the dike goes past the negative buoyancy horizon but that it sustains a swollen section within that horizon. Once it has gone through this horizon it takes a dimensionless distance of $\sim$10 for the dike to resume its steady state shape and velocity.

contrast to $\Delta\rho_+ = -1$ in that horizon and assume that material above and below correspond to the same density contrast of $\Delta\rho_o = 1$.

[33] Figure 15 shows how the dike penetrates a horizon with dimensionless thickness 2.84. As expected, the dike develops an inflated nose region and slows down markedly. In due time, however, the nose region rises above the low-density horizon, and its renewed buoyancy acts to increase flow velocities back to values that prevailed in the denser basement. As shown in Figure 16, however, the rate of propagation follows a complex evolution, such that it overshoots its steady state value as the swollen dike section deflates.

[34] The dike behavior depends strongly on the horizon thickness. The thicker the horizon, the larger the effect on the dike ascent rate and the larger the magma overpressure are (Figures 16–18). As discussed above, the effect is negligible when the horizon thickness is much smaller than the length of the dike nose, i.e. when L/L^* is less than about 0.1. The magma overpressure is largest in the low-density horizon and reaches its maximum when the dike tip leaves the horizon. This maximum value therefore increases with the thickness of the low-density horizon (Figure 18).

5.2. Two Layers With Negative Buoyancy

[35] With a single negative buoyancy layer, our calculations show that hydrostatic conditions prevail within that layer. One consequence is that the magma overpressure is largest at the interface between the two layers. The curvature of the dike walls is also largest at the interface, implying that the tension on the dike walls is also largest

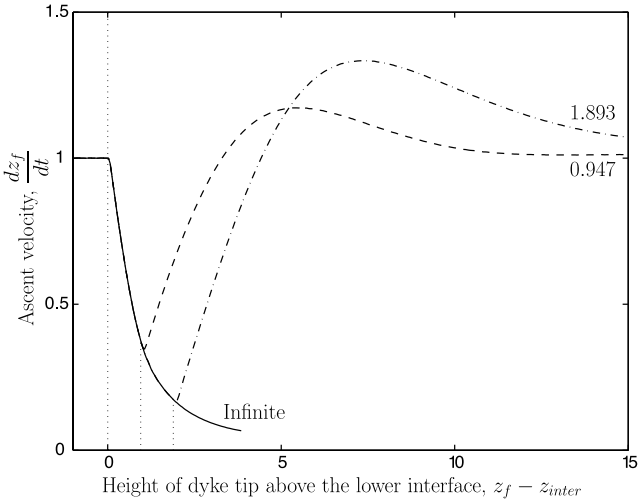

Figure 16. Ascent rate of a dike that goes through a negative buoyancy horizon. Each curve corresponds to a different horizon thickness L (whose dimensionless value is shown alongside the curve). Vertical dotted lines stand for the base and top of the horizon. Note that the dike accelerates as it leaves the low-density horizon and then decelerates as it adjusts to its steady state velocity in the layer above the horizon. These acceleration and deceleration phases are related to the inflation and deflation of the swollen dike section that develops in the horizon.

there. This predicts that the dike walls would fail at the interface if the overpressure is large enough.

[36] For more complicated stratified media, the pressure distribution and wall deformation may be different. We have considered, for example, two upper layers with increasing negative buoyancy (Figure 19). The density contrast takes values of $-1/4$ in the first layer of thickness 0.5 and -1 in the second layer, which is supposed to be semi-infinite. In this case, the dike is allowed to go through the first layer and penetrate into the second layer. The hydrostatic conditions that prevail in the swollen nose region dictate that the magma overpressure can only decrease in negative buoyancy layers and hence that it is largest at the dense basement interface. Due to the more complicated overpressure distribution, however, the dike develops its thickest section and the largest wall curvature above that interface, within the lower negative buoyancy layer (Figure 19). In this case, the largest tension on the dike walls is achieved above the basement interface, and this is where failure is most likely.

5.3. Minimum Thickness of Low Density Rocks for Sill Inception

[37] We have shown that a dike continues to rise even if magma becomes negatively buoyant above some interface. In this case, the dike develops a swollen nose region that straddles the interface as the internal magma pressure builds up. Tensile stresses that are generated in the encasing rocks may eventually overcome their strength. If this happens, we expect that magma induces fracturing in the horizontal direction and generates a sill, as illustrated in laboratory experiments [*Rivalta et al.*, 2005; *Kavanagh et al.*, 2006]. One must also imagine that, in reality, the dike extends over a finite horizontal distance and propagates laterally as it rises. Above the interface that separates dense basement and negative buoyancy layers, dike ascent slows down and the relative magnitudes of the horizontal and vertical components of propagation change in favour of the former. This behavior is illustrated in the experiments of *Lister and Kerr* [1991], where a dike that rises through material with a linear density decrease is seen to spread laterally at the neutral buoyancy level. This experimental dike also rises above the neutral buoyancy level, as in the present calculations, and hence also develops an overpressured and swollen nose region straddling that level. We conclude that a negative buoyancy layer may have two effects on magma ascent: sill inception at, or slightly above, the interface with dense basement and lateral spreading of the feeder dike in the vicinity of that interface.

[38] With one or several negative buoyancy layers, the magma overpressure increases with time as the dike con-

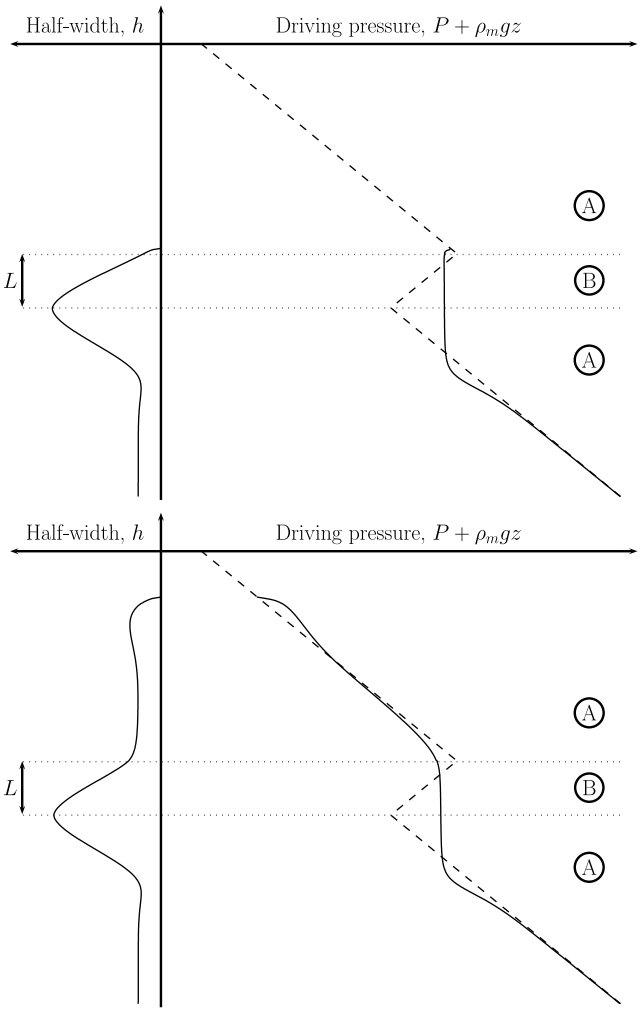

Figure 17. Width and driving pressure distribution in a dike that goes through a horizon with negative buoyancy (layer B, $L = 2.840$). Conventions are as in Figure 7. The upper and lower panels correspond to times (2) and (4) in Figure 15. Note that the driving pressure is almost constant within the swollen dike section that develops in the negative buoyancy horizon.

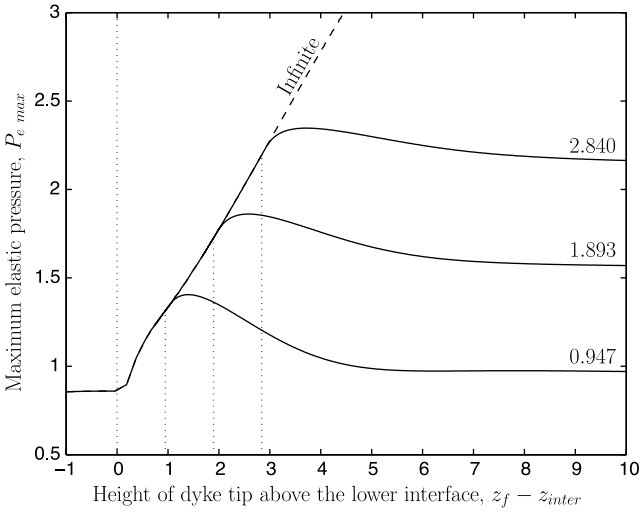

Figure 18. Maximum value of the magma overpressure ($P_{e\ \max}$) in a dike that goes through a negative buoyancy horizon as a function of the dike tip position. This pressure is achieved at the lower interface (i.e., at $z = z_{\text{inter}}$). It increases as the dike starts penetrating into the negative buoyancy horizon and then decreases as the dike leaves the horizon. Calculations are shown for different horizon thicknesses (whose values are indicated alongside the curves). Vertical dotted lines show the base and top of the horizons.

tinues to rise, albeit at a decreasing rate. The threshold for wall fracture may be reached if the dike is able to penetrate sufficiently far above the dense basement. This may not occur for two reasons. One is that the low-density layers are not thick enough, either because they lie at a shallow depth beneath Earth's surface, or because they are overlain by a dense layer where magma becomes buoyant again, as illustrated by Figure 1. A set of low-density layers that is not thick enough would allow the dike to pass through without a sill being formed. Another reason for the lack of a sill is that the deep source of magma becomes exhausted so that the dike stops propagating. For sill intrusion, therefore a necessary, but not sufficient condition, is that low-density layers exceed a certain cumulative threshold thickness noted L_c.

[39] We have shown that the pressure distribution in swollen dike sections is very close to being hydrostatic, and hence depends neither on the elastic properties of the encasing rocks nor on the magma flow rate. Thus a dike that extends over height l_T through a set of low-density layers develops overpressure $\Delta P_{e\ \max} \approx |\Delta\rho_+ g l_T|$ at the lower interface, where $\Delta\rho_+$ is now understood as the average density contrast for the set of layers (thickness weighted). This overpressure is applied to a curved interface and generates tensile stresses that are, in the geometrical configuration of an elongated fissure, of the same magnitude. The tensile strength of rocks is not known accurately and depends on the density of minor defects and microfissures. According to *Rubin* [1995], ΔP_c, the critical overpressure that is required to nucleate a new macroscopic fracture in crustal rocks, is about 50 MPa. This estimate should be considered as an upper bound for shallow crustal material that has been subjected to repeated cycles of deformation and fracturing. Using the systematics of discharge rate in three well-documented eruptions, one may deduce that the volcano reservoir pressure decreased by an amount in the 10–25 MPa range [*Stasiuk et al.*, 1993]. We may assume that these eruptions began when the reservoir roof ruptured, so that these pressure drop values provide estimates for ΔP_c. Allowing for the possibility that the interface between two layers may be weaker than these estimates, we consider values in the 5–10 MPa range, keeping in mind that they are probably underestimated. The fracture criterion $\Delta P_c \approx |\Delta\rho_+ g L_c|$ provides a relationship between the density contrast and threshold thickness L_c for sill inception (Figure 20).

[40] For common rock types, the negative density contrast $\Delta\rho_+$ between basaltic magma and sedimentary rocks is in the 100–400 kg m^{-3} range (Table 1, see also Figure 1 and gravity studies summarized by *Corry* [1988]). In some cases, magma intrudes young sedimentary layers that are not fully compacted and lithified. This is expected in initial tectonic phases of extension, when lithosphere thinning induces decompression melting and magma rises toward sedimentary packages that have not yet accumulated over a large thickness. Examples may be found in the Silurian rocks of Ireland, where the Cill Brid sills intruded a weakly consolidated sedimentary pile [*Mohr*, 1990]. Another example is provided by the Newfoundland continental margin, where recent drilling went through two diabase sills only 100–200 m above basement [*Tucholke et al.*, 2004]. These sills intruded poorly consolidated sediments when the seafloor was at relatively shallow depth. Representative density values for these sedimentary packages are in a 1.9–2.1 $\times$ 10^3 kg m^{-3} range [*Tucholke et al.*, 2004].

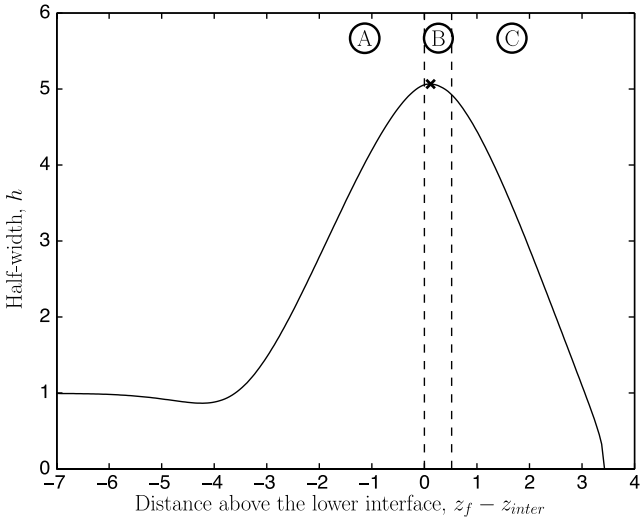

Figure 19. Width of a dike that has gone through two layers with increasingly negative buoyancy. Density contrasts for layers A, B, C are as follows: $\Delta\rho_A/\Delta\rho_o = 1$, $\Delta\rho_B/\Delta\rho_o = -1/4$, $\Delta\rho_C/\Delta\rho_o = -1$. The two interfaces separating these layers are shown by vertical dashed lines. The dike is widest, and the wall curvature is largest at an intermediate level (indicated by a star symbol) and not at the dense basement interface beneath the low-density cover. Using parameters quoted in the text, this occurs at about 200 m above the basement interface.

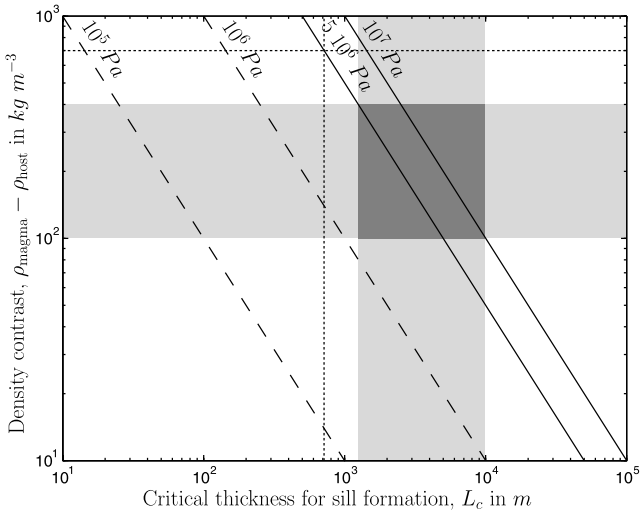

Figure 20. Minimum thickness of an upper layer with negative buoyancy for the development of a critical magma overpressure for sill inception within the dike. At the critical value of the overpressure, magma breaches the dike walls and feeds a horizontally propagating sill. Curves are shown for different values of the critical overpressure. Typical values for the density contrast between magma and host rocks are shaded in gray. The horizontal dotted line indicates the maximum density contrast, which may be achieved in poorly consolidated and compacted sedimentary rocks. The solid lines stand for the estimated range for the critical magma overpressure required for sill inception.

In such cases, therefore the negative density contrast between basaltic magma and surroundings may be as large as 700 kg m^{-3}.

[41] Using the ranges of 5–10 MPa and 100–400 kg m^{-3} for ΔP_c and $\Delta\rho_+$, respectively, we obtain that the minimum thickness of low-density rocks for sill inception is about 1 km. This minimum thickness may be as low as 700 m for young sedimentary material that is not fully lithified (Figure 20). These results are best appreciated with respect to Figure 1, which shows the vertical density distribution through the Michigan basin sedimentary strata from *Hinze et al.* [1978]. These data indicate that many sedimentary rocks may in fact be denser than, or almost as dense as, basalt. The lower bound of 1 km for the thickness of low-density rocks quoted above was obtained for a large density contrast which is only achieved in dry consolidated sedimentary layers in exceptional circumstances (Figure 1). For a representative average density contrast of 200 kg m^{-3}, the minimum thickness is 2 km. For the particular case of the Michigan basin, a basaltic sill could not be generated near the basement/cover interface because the low-density sedimentary layers that are found there extend only over a few hundred meters. Sill inception would be most likely near the middle of the sedimentary pile, at a depth of about 2 km, where the lowest densities are recorded (2200 kg m^{-3}).

5.4. Discussion

[42] Our calculations rely on several simplifying assumptions that deserve discussion. We have not accounted for slippage between two layers, which may favor sill inception. Many sills are found along bedding planes [*Francis*, 1982], which may suggest such a control. We have shown, however, that the largest internal overpressure is reached at the base of low-density strata, which also favors lateral intrusion at a bedding plane. If slippage was a key process, one would expect that it is associated with specific lithological associations, for example, at the interface separating a soft layer and a stiffer one above. This does not appear to be so. *Francis* [1982], for example, found that no particular lithology determines the intrusion level in the Carboniferous strata of northern Britain.

[43] Another assumption made in this study is that dikes are fed at a steady rate. In reality, one may expect that the flow rate wanes as the deep magma source gets exhausted, as observed, for example, through the yearlong Laki eruption in Iceland [*Thordarson and Self*, 1993]. In this case, only a fixed volume of magma is available, which may not allow the development of a very large inflated region at the interface between dense basement and low-density cover. Before reaching such an interface, a dike whose supply has been cut off will maintain an approximately constant magma volume in its nose region and will slow down as its tail region extends vertically and thins [*Roper and Lister*, 2007]. Once the dike tip has crossed the interface, the tail will continue to feed magma to the top of the dense basement. The tail region will adopt a different shape than that for a steady magma flux, but it will still be such that magma buoyancy is balanced by viscous forces, and hence will not contribute to the force budget in the vicinity of the interface. Eventually, the total volume of magma injected will find its way to the interface, save for losses due to solidification against the dike walls. The overpressure that develops at the interface is set by the vertical extent of the inflated region that extends above the interface, which itself depends on the amount of magma that is available. In this case, therefore the total volume of magma may be a limiting factor for the inception of a sill.

5.5. Density Versus Rigidity Control on Sill Emplacement

[44] In laboratory experiments of hydraulic fracturing through two layers, *Kavanagh et al.* [2006] were not able to generate sills by a density inversion (i.e. such that magma is negatively buoyant in the upper layer). They carried out only one experiment with that particular configuration and observed that the experimental dike propagated through the interface and eventually rose to the surface. They therefore suggested that sill inception is more likely due to a strong rigidity contrast, such that dike penetration into a rigid upper layer is hampered or altogether prevented.

[45] A key control on sill inception is the magnitude of the magma overpressure that can be generated during propagation. Indeed, one limitation of the *Kavanagh et al.* [2006] experiments is that the magma overpressure was set at arbitrary values. We note that the only experiment that had a density inversion involved an upper layer of small thickness, such that the magma overpressure could not rise to large values. In reality, as emphasized by our calculations and the analysis by *Lister* [1990, 1991], magma overpressure is generated only in the nose region of the dike and hence is determined by the vertical extent of that region (note that this statement is true even in material with very

large fracture toughness). Our calculations have shown that ascent through a density inversion is an efficient way to generate large overpressures. We do not dispute that a very strong rigidity contrast will induce sill inception, but argue that the role of a density inversion is probably more important in many geological cases. The ideal test would be to find the different configurations in the field and to associate sills with only one of them, but this cannot be done easily. One reason is that identification of a rock type, such as sandstone, for example, is not sufficient to specify its physical properties in a reliable manner because of the large spread of values that exists (Table 1). Within the Michigan basin sedimentary strata, for example, the densities of the various sandstone layers range from 2.48×10^3 to 2.72×10^3 kg m^{-3} [*Hinze et al.*, 1978], which makes some of them denser than basaltic melts. Thus the physical properties of country rock must be determined on a case by case basis, which requires a dedicated effort outside the scope of the present paper. To get round this difficulty, we discuss below several observations which shed light on sill emplacement characteristics. *Kavanagh et al.* [2006] were interested in sills that are generated deep in the continental crust and attributed part of the rigidity contrast to weakening of lower crustal environments by prolonged heating and hydration. Most observations, however, deal with upper crustal levels.

[46] In the Henry Mountains, Utah, several sills of Eocene age intrude Triassic and Jurassic sedimentary rocks over a depth interval of ≈800 m, about 2.5 km above the Precambrian crystalline basement [*Johnson and Pollard*, 1973]. The Sawtooth Ridge sill is found within a sandstone formation. Lower down in the sequence, the Trachyte Mesa sill intrudes a shaly horizon within a thick sandstone unit. The deepest sill, called Buckhorn Ridge, lies in the upper part of a sequence of thin sandstones and shales, below a massive sandstone layer. We note that the magma batch that fed the uppermost sill was able to go through several massive sandstone layers and furthermore that sandstones and shales do not differ greatly in their elastic moduli (Table 1). Interestingly, several vertical intrusions are found above the roof of the Trachyte Mesa sill [*Johnson and Pollard*, 1973], indicating again that magma was able to rise past this intermediate level of sill inception. In the Henry Mountains area, therefore some sills are found within a sedimentary formation and no particular lithology acts as a barrier to dike ascent. These observations are strongly reminiscent of those of *Francis* [1982] on the sills of northern Britain.

[47] As regards density, it is clear that many sills are found within sedimentary rocks just above crystalline basement, where a major density inversion is expected to occur. We have already discussed two such cases, in the Silurian rocks of Ireland [*Mohr*, 1990] and the Newfoundland continental margin [*Tucholke et al.*, 2004]. The density relationship between magma and host rocks is established beyond doubt by load structures at the sill bases in the former case and by density measurements in the latter one. Incidentally, in these cases involving young sedimentary packages that were not fully lithified yet, there was no rigid layer to impede or prevent magma ascent. More generally, *Corry* [1988] noted that all the basaltic sills and laccoliths that he could find data for are associated with positive gravity anomalies and positive density contrasts (after corrections for post-emplacement cooling and crystallization). This shows that the basaltic melts were intruded in rocks that were less dense than them, as in our proposed scenario.

[48] In a discussion on the dominant physical control on the level of sill intrusion, the most important point perhaps rests in the difference between the local physical properties of specific lithologies and the large-scale impact of a rock layer on dike ascent, which depends on its thickness. Focussing on rigidity or density may not be sufficient to account for dike behavior, which depends on a buoyancy force developed over a finite nose length and hence a finite thickness of country rock. Discussing the observation by *Du Toit* [1920] and *Mudge* [1968] that the bases of thick mudstones are preferred horizons for dolerite sills in some regions, *Francis* [1982] emphasized that this does not apply to the sills of northern Britain. He proposed that none of the British Carboniferous mudstones were thick enough to have exerted that kind of control on magma emplacement. Our calculations support this suggestion.

6. Conclusions

[49] Numerical calculations of dike propagation through layered rocks emphasize that penetration through low-density rocks is determined by local buoyancy considerations in the swollen nose region, independently of the total buoyancy of the magma column integrated from source to tip. For magma to develop an overpressure that is large enough to induce lateral failure of the dike walls, it must penetrate through a minimum thickness of low-density material. Wall deformation may follow complicated patterns in a pile of layered rocks, such that sill inception may occur above the interface between dense basement rocks and low-density superficial assemblages.

[50] In more general terms, our results show that dike propagation may proceed in a complex manner due to transient swell and pinch behavior near an interface between two layers with different densities. The ascent rate may change over distances of a few kilometers without any change of magma composition or supply rate.

Appendix A: Deformation Regime in the Nose Region of a Dike

[51] As shown by *Lister* [1990] and *Lister and Kerr* [1991], a simple method to evaluate dike behavior is to consider the main force balance in the tail and nose regions. In both regions, the driving force is magma buoyancy and one must determine the dominant resistance to propagation. Three types of stress are involved: viscous stresses associated with magma flow, elastic stresses driving country rock deformation and finally stresses that sustain fracturing at the tip. In the long tail region, away from the dike tip, it takes small elastic stresses to maintain an open fracture and the dominant force balance is between magma buoyancy and viscous head loss. As shown in the main text, this introduces a scale for the dike width noted h^*. Near the tip, there must be a significant magma overpressure to generate the large stresses that are required for fracturing. Thus the nose

region must be wider than the tail region in order to diminish the magnitude of viscous stresses. We may thus consider two different force balances in the nose, depending on the dominant resistance to propagation. One may consider that fracturing is the limiting process, such that magma buoyancy generates stresses that are large enough to overcome the fracture toughness of rock. This defines one scale length, L_f, such that:

$$K_c = \Delta P\sqrt{L_f} = \Delta\rho g L_f^{3/2}, \tag{A1}$$

where K_c is the toughness and ΔP is the magma overpressure in the nose. Solving for L_f, we find that:

$$L_f = \left(\frac{K_c}{\Delta\rho g}\right)^{2/3}. \tag{A2}$$

The alternative possibility is that the main impediment to dike propagation is elastic deformation in the nose region. In this case, the dominant force balance in that region is between buoyancy and the overpressure required to open up a fracture of width h^*. This defines a second length-scale, noted L^* (equation (17)).

[52] In dimensionless form, the governing equations for dike propagation involve a single dimensionless number that characterizes the deformation regime of the dike nose. This number can be interpreted as the ratio between two different length-scales or the ratio between two toughness scales. From the two length-scales defined above, we obtain:

$$\frac{L_f}{L^*} = \left[\frac{K_c}{\Delta\rho g {L^*}^{3/2}}\right]^{2/3} = \left[\frac{K_c}{\left(\frac{G^3}{(1-\nu)^3}\frac{3\mu Q}{2}\right)^{1/4}}\right]^{2/3}. \tag{A3}$$

This can also be written as a function of a dimensionless toughness ratio such that:

$$\frac{L_f}{L^*} = \left(\frac{K_c}{K^*}\right)^{2/3}, \tag{A4}$$

where K^* is a toughness scale associated with viscous flow requirements (*Lister* [1990] and equation (18)):

$$K^* = \Delta\rho g (L^*)^{3/2} = \left(\frac{G^3}{(1-\nu)^3}\frac{3\mu Q}{2}\right)^{1/4}. \tag{A5}$$

It should be noted that this toughness scale does not depend on the buoyancy of magma.

[53] The dominant resistance to propagation dictates the magnitude of the buoyancy force in the nose region and hence the length of that region. In turn, this sets the relevant length-scale for the equations of motion. If $L_f/L^* \gg 1$, or if $K_c/K^* \gg 1$, corresponding to large rock toughness, elastic deformation is not a limiting factor and buoyancy must be accumulated over length L_f to overcome the resistance to fracture. In this case, the proper length-scale is L_f. In the other limit, for $L_f/L^* \ll 1$ or $K_c/K^* \ll 1$, it is the elastic opening of the fracture that requires the largest stresses, and one should scale length with L^*. In both cases, the tail region is in the same dynamical regime characterized by a balance between buoyancy and viscous forces, which emphasizes the fundamental role played by the nose region. *Roper and Lister* [2007] have demonstrated that for $K_c/K^* < 2$, the nose region is such that its length scales with the viscous length-scale, L^*, and such that its width is comparable to h^*, the width of the tail region (see Figure C2 in Appendix C). As shown by Figure C2 in Appendix C, the nose extends over a length of $\approx 4 \times L^*$ in this regime, independently of the toughness ratio and hence independently of the fracture toughness of encasing rocks. For $K_c/K^* > \approx 2$, the length of the nose region is much larger, as expected. The asymptotic limit such that the nose length scales with L_f is reached for $K_c/K^* > \approx 8$. In this limit, the width of the nose region deviates markedly from that of the tail.

[54] In order to determine in which dynamical regime true dikes propagate, we focus on basaltic magmas. Typical values of the relevant physical properties and control variables are $\nu = 0.2$, $\mu = 10^2$ Pa s and $Q = 2$ m^3 s^{-1} m^{-1} [*Thordarson and Self*, 1993]. As shown by Table 1, $G \approx 10^{10}$ Pa. From these, we find that $K^* \approx 150$ MPa m$^{1/2}$, as *Lister and Kerr* [1991]. One should note that this estimate is weakly sensitive to the various inputs because of the small power law dependence involved and does not depend on magma buoyancy at all (see equation (A5)). Values of the fracture toughness have been measured on rock samples in the laboratory [*Atkinson and Meredith*, 1987] and deduced from the dimensions of dikes (breadth and thickness) in the field [*Delaney and Pollard*, 1981]. The two methods indicate values of about 1 and 100 MPa m$^{1/2}$, respectively. This large discrepancy has not been explained and we shall allow for values within this whole range. We thus obtain that $6 \times 10^{-3} < K_c/K^* < 7 \times 10^{-1}$ for basaltic dikes, which shows that the proper length-scale is L^*, reflecting the fact that the dominant dynamical balance in the nose region is between buoyancy and elastic stresses. As shown by *Roper and Lister* [2007], many laboratory experiments on hydraulic fracturing are in the other regime, such that $K_c/K^* \gg 1$.

Appendix B: Numerical Method

[55] To ensure numerical stability, we have developed a numerical code relying on a semi-implicit method. The dimensionless continuity equation is written as follows:

$$\left.\frac{\partial h}{\partial t}\right|_k = -\frac{1}{2}\left(\left.\frac{\partial \phi}{\partial z}\right|_k^t + \left.\frac{\partial \phi}{\partial z}\right|_k^{t+1}\right), \tag{B1}$$

where $\phi|_k^t$ stands for the local magma flux at height z_k and time t. Note the difference with the dimensional version (equation (6)): a factor of 2 disappears due to the scalings for h, ϕ and z. As shown by equation (3), the magma flux depends on the dike width and internal magma pressure. As we march forward in time, we seek to write this flux at time $t + \Delta t$ as a function of the unknown dike width h^{t+1} and internal magma pressure P_e^{t+1}. To implement the implicit method, we recast the problem in terms of single unknown

variable, h^{t+1}, which requires a relationship between h^{t+1} and P_e^{t+1}.

B1. Relationship Between Dike Width and Internal Overpressure

[56] We calculate the elastic pressure component and the dike width over a discrete grid extending from some initial depth z_1 to the dike tip at $z = z_f$. Linear elastic fracture mechanics theory dictates that:

$$h_i = \frac{1}{\pi}\left\{\sum_{k=1}^{n-2}\int_{z_k}^{z_{k+1}} k(z_f, z_i, \xi)P_e(\xi)d\xi + \int_{z_{n-1}}^{z_f} k(z_f, z_i, \xi)P_e(\xi)d\xi\right\}, \tag{B2}$$

$$K_c\sqrt{2} = \frac{2}{\pi}\left\{\sum_{k=1}^{n-2}\int_{z_k}^{z_{k+1}} \frac{P_e(\xi)}{\sqrt{z_f-\xi}}d\xi + \int_{z_{n-1}}^{z_f} \frac{P_e(\xi)}{\sqrt{z_f-\xi}}d\xi\right\}, \tag{B3}$$

where h_i is the dike width at $z = z_i$. The pressure variation between two grid points is assumed to be linear:

$$P_e(z_k < \xi < z_{k+1}) = P_{ek} + (\xi - z_k)\frac{P_{ek+1} - P_{ek}}{\Delta z}. \tag{B4}$$

This is not a very good approximation near the dike tip, where the pressure distribution has a singularity. Thus the value of pressure that is calculated at $z = z_f$ is not reliable and we calculate the near-tip dike width, using the local approximation $h \sim K_c\sqrt{2(z_f - z)}$. As discussed by *Mériaux and Jaupart* [1998], near-tip errors only perturb the solutions over a very small distance.

[57] Using the equations above, we obtain a linear relationship between the two sets of values for width and pressure, which is written in matrix form:

$$\begin{pmatrix} h_1 \\ h_i \\ h_{n-1} \\ K_f\sqrt{2} \end{pmatrix} = \begin{pmatrix} M_{1,k} \\ M_{i,k} \\ M_{n-1,k} \\ M_{n,k} \end{pmatrix} \begin{pmatrix} P_{e1} \\ P_{ek} \\ P_{en-1} \\ P_{ef} \end{pmatrix}. \tag{B5}$$

[58] Note that the last row does not involve the dike width at $z = z_f$, which is zero by definition, but the boundary condition involving the fracture toughness (equation (B3)). This matrix relationship can be inverted to calculate pressure as a function of dike width.

B2. Accuracy

[59] In order to assess the accuracy of this scheme, we have used an analytical solution for the width of a fracture which is kept open by a unit overpressure applied over length λ at the tip:

$$\Delta P_e = 1 \text{ for } z_f - \lambda < z < z_f. \tag{B6}$$

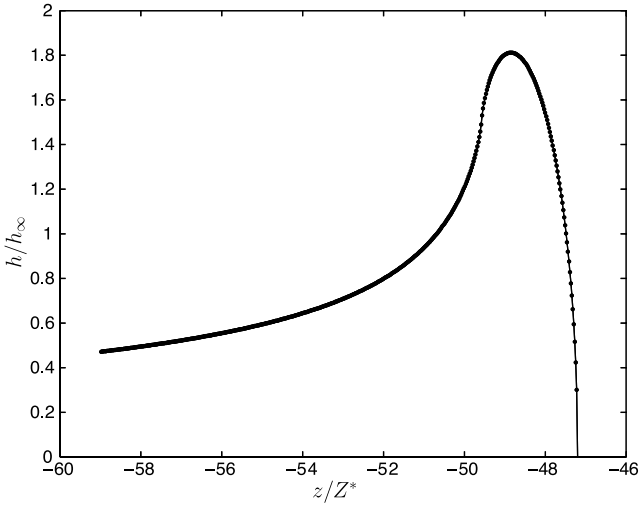

Figure B1. Fracture width as a function of distance in dimensionless values for a unit pressure applied over distance $\lambda = 2.36$ at the fracture tip (see equation (B6)). Solid curve: theoretical curve (equation (B8)). Dots: calculated values over a discrete grid using the matrix formulation of the elastic problem (equation (B5)).

From equation (9), we deduce that:

$$h(z) = \frac{1}{\pi}\int_{z_f-\lambda}^{z_f} k(z_f, z, \xi)d\xi, \tag{B7}$$

integration leads to:

$$h(z) = \frac{\Delta P_e}{\pi}\left[2\sqrt{\lambda(z_f - z)} - (z_f - \lambda - z) \cdot \ln\left|\frac{\sqrt{z_f - \lambda - z} + \sqrt{\lambda}}{\sqrt{z_f - \lambda - z} - \sqrt{\lambda}}\right|\right]. \tag{B8}$$

[60] Figure B1 compares the analytical solution to that obtained over a discrete grid using the matrix formulation (equation (B5)).

[61] These calculations are done over a known depth interval. In practice, however, the dike propagates over a finite distance between two time steps and one of the unknowns is the tip position z_f. From the continuity equation, we obtain the dike width at time $t + 1$ and need to solve for the corresponding pressure distribution. Matrix $\underline{\underline{M}}$ must therefore be rewritten in order to involve the change of tip position between times t and $t + 1$. We consider the small increments:

$$h^{t+1} = h^t + \delta h \tag{B9}$$

$$P_e^{t+1} = P_e^t + \delta P_e \tag{B10}$$

$$z_f^{t+1} = z_f^t + \delta z_f. \tag{B11}$$

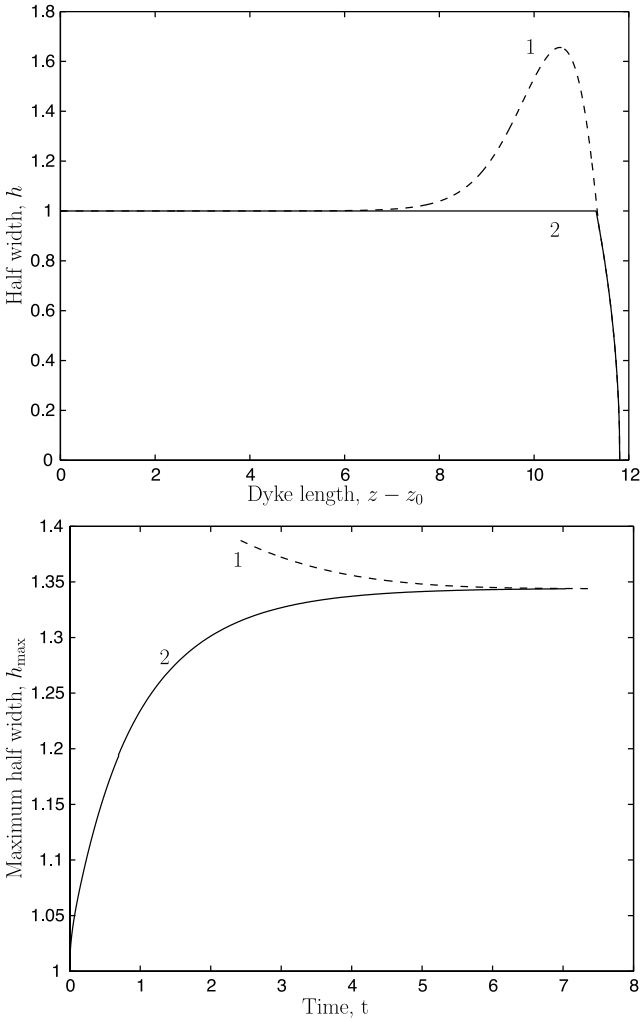

Figure C1. Convergence tests for the numerical scheme and for a fixed magma flux into the dike. All variables are shown in dimensionless values. (top) Two different initial dike shapes. (bottom) Maximum dike width as a function of time for the two initial conditions for $\Delta z = 5.9 \times 10^{-3}$ and $K_c/K^* = 1$. Here time is measured with respect to the initial condition (top) . Both sets of results tend to the same value, which is within 4% of the analytical result of *Lister* [1990].

Substituting into $\underline{h}^{t+1} = \underline{\underline{M}}^{t+1}\underline{P_e}^{t+1}$ and linearizing leads to the following equations:

$$\begin{pmatrix} h_1^{t+1} \\ \vdots \\ h_{n-1}^{t+1} \\ K_c\sqrt{2} \end{pmatrix} = \underline{\underline{M_1}} \begin{pmatrix} P_{e1}^{t+1} \\ \vdots \\ P_{en-1}^{t+1} \\ P_{ef}^{t+1} \end{pmatrix} + \delta z_f \underbrace{\underline{\underline{M_2}} \begin{pmatrix} P_{e1}^{t} \\ \vdots \\ P_{en-1}^{t} \\ P_{ef}^{t} \end{pmatrix}}_{\underline{V_2}}, \tag{B12}$$

$$\begin{pmatrix} P_{e1}^{t+1} \\ \vdots \\ P_{en-1}^{t+1} \\ P_{ef}^{t+1} \end{pmatrix} = \underline{\underline{M_1}}^{-1} \begin{pmatrix} h_1^{t+1} \\ \vdots \\ h_{n-1}^{t+1} \\ K_c\sqrt{2} \end{pmatrix} - \delta z_f \underline{\underline{M_1}}^{-1} \underline{V_2}. \tag{B13}$$

B3. Numerical Scheme

[62] We rewrite these equations using h^{t+1} and δz_f:

$$\begin{pmatrix} P_{e1}^{t+1} \\ \vdots \\ P_{en-1}^{t+1} \\ P_{ef}^{t+1} \end{pmatrix} = \underline{\underline{LS}} \begin{pmatrix} h_1^{t+1} \\ \vdots \\ h_{n-1}^{t+1} \\ \delta z_f \end{pmatrix} + \underline{V}, \tag{B14}$$

which provides a relationship between the n values of pressure and an array of n values made of $(n-1)$ values of dike width and the tip position increment δz_f. By construction, the dike tip is located above the last grid point, such that $z_f > z_n$, and we solve for z_f.

[63] The continuity equation is used for $2 \le k \le (n-2)$. For $k = 1$ and $k = n-1$, we use two additional constraints provided by the boundary conditions. We impose a fixed volume flux at the base of the domain:

$$\phi|_1^{t+1} = Q \ (= 1 \text{ in dimensionless value}). \tag{B15}$$

Near the tip, we use the local approximation to the dike shape:

$$h_{n-1}^{t+1} = K_c\sqrt{2}\sqrt{z_f^{t+1} - z_{n-1}}. \tag{B16}$$

One additional equation is required for the tip position and we use volume conservation for a near-tip domain between $z = z_{n-2}$ and $z = z_f$:

$$\frac{\phi_{n-2}^{t+1} + \phi_{n-2}^{t}}{2} = \frac{V_{tip}^{t+1} - V_{tip}^{t}}{\Delta t}, \tag{B17}$$

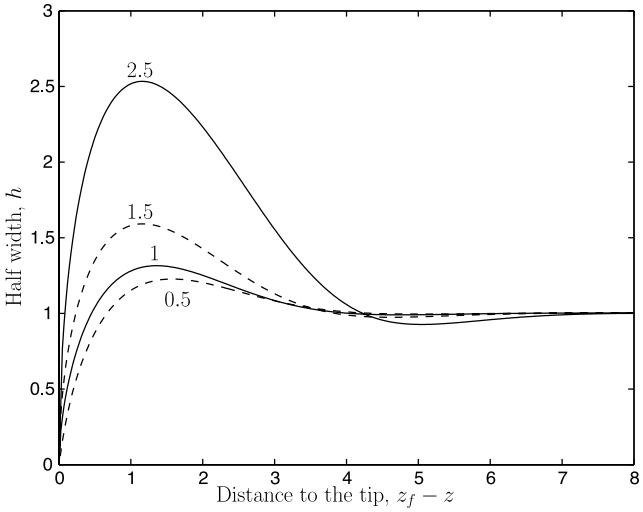

Figure C2. Calculated dimensionless steady state dike shapes for a fixed flux and different values of dimensionless stress intensity factor K_c/K^*, whose values are given along the curves. Results were obtained for $\Delta z = 2.36 \times 10^{-2}$.

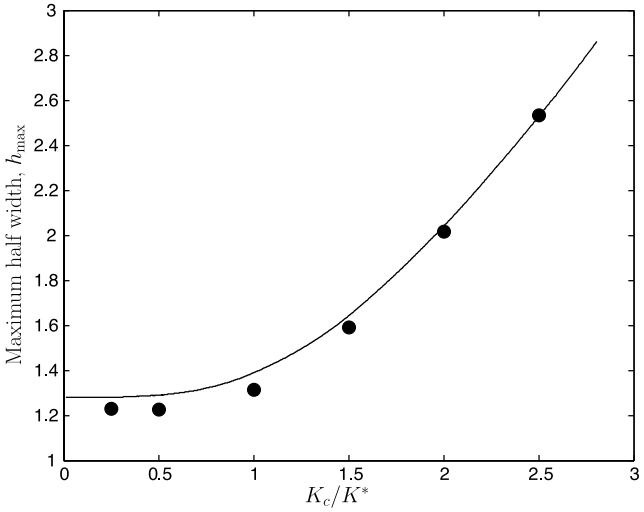

Figure C3. Maximum dike width as a function of dimensionless stress intensity factor K_c/K^* for steady state dikes fed at a constant rate. Solid curve: analytical results of *Lister* [1990]. Dots: numerical results for $\Delta z = 2.36 \times 10^{-2}$. The difference between numerical and analytical results is less than 4% everywhere.

where the volume of the tip region is calculated as follows:

$$V_{tip} = \int_{z_{n-2}}^{z_f - 2\Delta z} h(\xi)\, d\xi + \int_{z_f - 2\Delta z}^{z_f} K_c \sqrt{2} \sqrt{z_f - \xi}\, d\xi. \quad \text{(B18)}$$

We can also use volume conservation equation over the dike as a whole:

$$\int_{z_1}^{z_f^{t+1}} h^{t+1}(\xi)\, d\xi = Q\Delta t + \int_{z_1}^{z_f^t} h^t(\xi)\, d\xi. \quad \text{(B19)}$$

Comparing results obtained with these two different constraints allows an accuracy test.

[64] We thus obtain an equation for the unknowns h^{t+1} and δz_f:

$$\underline{\underline{MI}}.\left(h_{1\to n-1}^{t+1},\ \delta z_f\right) = \underline{NS_{sol}}. \quad \text{(B20)}$$

Appendix C: Convergence Tests

[65] We assess the performance of our numerical code through a comparison with the semi-analytical results of *Lister* [1990] for steady state dike propagation through an infinite homogeneous elastic medium.

[66] All calculations require an initial condition with a finite magma volume present over a finite distance. We have tested that solutions become independent of this condition once they have extended over a finite distance. Two different initial conditions were used (Figure C1a), one corresponding to an approximate dike shape close to those of *Lister* [1990], and the other corresponding to flat fissure ending abruptly. Calculations of the maximum dike width (in the nose region) are shown in Figure C1b for $K_c/K^* = 1$ and $\Delta z = 5.9 \times 10^{-3}$. The two calculations converge to the same value of 1.34, which is within 4% of the value obtained by *Lister* [1990].

[67] The shape of the dike is shown in Figure C2 for different values of the stress intensity factor K_c/K^* and $\Delta z = 2.36 \times 10^{-2}$. For further evaluation, we show on Figure C3 values of the maximum dike width, which is achieved in the bulbous nose region, as a function of K_c/K^*. Differences with the analytical results of *Lister* [1990] are less than 4% in all cases. Better agreement with the analytical results can be obtained with a finer grid spacing at the expense of extra computation time. Calculations shown in this paper are carried with grid spacings $\Delta z = 2.36 \times 10^{-2}$ or $\Delta z = 4.72 \times 10^{-2}$.

[68] **Acknowledgments.** We thank IPGP for financial support (contribution 2521). Careful comments and criticisms by Ross C. Kerr, Patrick McGovern, and an anonymous reviewer led to substantial improvement.

References

Atkinson, B. K., and P. G. Meredith (1987), Experimental fracture mechanics data for rocks and minerals, in *Fracture Mechanics of Rocks*, edited by B. K. Atkinson, chap. 11, pp. 477–525, Academic, London, U. K.

Baer, G. (1991), Mechanisms of dike propagation in layered rocks and in massive, porous sedimentary rocks, *J. Geophys. Res.*, *96*, 11,911–11,929.

Bonafede, M., and E. Rivalta (1999), On tensile cracks close to and across the interface between two welded elastic half-spaces, *Geophys. J. Int.*, *138*, 410–434.

Corry, C. (1988), Laccoliths: Mechanics of emplacement and growth, *Geol. Soc. Am. Spec. Pap.*, *220*, Geol. Soc. of Am., Boulder, Colo.

Delaney, P. T., and D. D. Pollard (1981), Deformation of host rocks and flow of magma during growth of minette dikes and breccia-bearing intrusions near Ship Rock, New Mexico, *U.S. Geol. Surv. Prof. Paper 1220*, 61 pp., U.S. Geol. Surv., Reston, Va.

Du Toit, A. L. (1920), The Karoo dolerites of South Africa: A study in hypabissal injection, *Trans. Proc. Geol. Soc. South Afr.*, *23*, 1–42.

Francis, E. (1982), Magma and sediment: I. Emplacement mechanism of late Carboniferous tholeiite sills in northern Britain, *J. Geol. Soc. Lond.*, *139*, 1–20.

Gudmundsson, A. (2005), The effects of layering and local stresses in composite volcanoes on dyke emplacement and volcanic hazards, *Geodynamics*, *337*, 1216–1222.

Gudmundsson, A., and S. L. Brenner (2001), How hydrofractures become arrested, *Terra Nova*, *13*, 456–462.

Gudmundsson, A., and S. L. Philipp (2006), How local stress fields prevent volcanic eruptions, *J. Volcanol. Geotherm. Res.*, *158*, 257–268.

Hinze, W., J. Bradley, and A. Brown (1978), Gravimeter survey in the Michigan basin deep borehole, *J. Geophys. Res.*, *83*, 5864–5868.

Johnson, A., and D. Pollard (1973), Mechanics of growth of some laccolithic intrusions in the Henry mountains, Utah: I. Field observations, Gilbert's model, physical properties and flow of the magma, *Tectonophysics*, *18*, 261–309.

Kavanagh, J. L., T. Menand, and R. S. J. Sparks (2006), An experimental investigation of sill formation and propagation in layered elastic media, *Earth Planet. Sci. Lett.*, *245*, 799–813.

Lister, J. R. (1990), Buoyancy-driven fluid fracture: The effects of material toughness and of low-viscosity precursors, *J. Fluid Mech.*, *210*, 263–280.

Lister, J. R. (1991), Steady solutions for feeder dykes in a density-stratified lithosphere, *Earth Planet. Sci. Lett.*, *107*, 233–242.

Lister, J. R., and R. C. Kerr (1991), Fluid-mechanical models of crack propagation and their application to magma transport in dykes, *J. Geophys. Res.*, *96*, 10,049–10,077.

Menand, T., and S. R. Tait (2002), The propagation of a buoyant liquid-filled fissure from a source under constant pressure: An experimental approach, *J. Geophys. Res.*, *107*(B11), 2306, doi:10.1029/2001JB000589.

Mériaux, C., and C. Jaupart (1998), Dike propagation through an elastic plate, *J. Geophys. Res.*, *103*, 18,295–18,314.

Mohr, P. (1990), Late Caledonian dolrite sills from SW Connacht, Ireland, *J. Geol. Soc. Lond.*, *147*, 1061–1068.

Mudge, M. (1968), Depth control of some concordant intrusions, *Bull. Geol. Soc. Am.*, *79*, 315–332.

Muskhelishvili, N. I. (1953), *Some Basic Problems of the Mathematical Theory of Elasticity*, P. Noordhoff Ltd., Groningen, Netherlands.

Rivalta, E., M. Böttinger, and T. Dahm (2005), Buoyancy-driven fracture ascent: Experiments in layered gelatine, *J. Volcanol. Geotherm. Res.*, *144*, 273–285.

Roper, S. M., and J. R. Lister (2007), Buoyancy-driven crack propagation: The limit of large fracture toughness, *J. Fluid Mech.*, *580*, 359–380.

Rubin, A. M. (1995), Propagation of magma-filled cracks, *Ann. Rev. Earth Planet. Sci.*, *23*, 287–336.

Spence, D. A., P. W. Sharp, and D. L. Turcotte (1987), Buoyancy-driven crack propagation: A mechanism for magma migration, *J. Fluid Mech.*, *174*, 135–153.

Stasiuk, M. V., C. Jaupart, and R. S. J. Sparks (1993), On the variations of flow rate in non-explosive lava eruptions, *Earth Planet. Sci. Lett.*, *114*, 505–516.

Thordarson, T., and S. Self (1993), The Laki (Skaftár Fires) and Grímsvötn, *Bull. Volcanol.*, *55*, 233–263.

Touloukian, Y. S., and C. Y. Ho (1981), *Physical Properties of Rocks and Minerals*, McGraw-Hill, New York.

Tucholke, B., et al. (2004), Shipboard scientific party, 2004, site 1276, in *Proc. ODP*, *Init. Repts.*, vol. 210, pp. 1–358, Ocean Drilling Program, College Station, Tex.

Weertman, J. (1971), Theory of water-filled crevasses in glaciers applied to vertical magma transport beneath oceanic ridges, *J. Geophys. Res.*, *76*, 1171–1183.

C. Jaupart and B. Taisne, Equipe de Dynamique des Fluides Géologiques, Institut de Physique du Globe de Paris, 4, Tour 14–15, place Jussieu, F-75252 Paris CEDEX 05, France. (taisne@ipgp.jussieu.fr)